# Friction Regimes of Water-Lubricated Diamond (111): Role of Interfacial Ether Groups and Tribo-Induced Aromatic Surface Reconstructions

Takuya Kuwahara,[1] Gianpietro Moras,[1] and Michael Moseler[1,2,*]
[1]Fraunhofer IWM, MicroTribology Center μTC, Wöhlerstraße 11, 79108 Freiburg, Germany
[2]Institute of Physics, University of Freiburg, Hermann-Herder-Straße 3, 79104 Freiburg, Germany
(Received 2 May 2017; revised manuscript received 25 July 2017; published 31 August 2017)

Large-scale quantum molecular dynamics of water-lubricated diamond (111) surfaces in sliding contact reveals multiple friction regimes. While water starvation causes amorphization of the tribological interface, small $H_2O$ traces are sufficient to preserve crystallinity. This can result in high friction due to cold welding via ether groups or in ultralow friction due to aromatic surface passivation triggered by tribo-induced Pandey reconstruction. At higher water coverage, Grotthuss-type diffusion and $H_2O$ dissociation yield dense H/OH surface passivation leading to another ultralow friction regime.

DOI: 10.1103/PhysRevLett.119.096101

Exceptional mechanical properties, high chemical stability, and thermal conductivity make diamond an ideal candidate for applications where a material has to withstand severe tribological conditions. Examples of such applications include the machining of rocks [1] and nonferrous materials [2], the mechanical polishing of diamond gems [3], and bearings that operate in highly abrasive environments [4]. Facilitated by the advancement in growth [5,6] and polishing techniques [7,8], the use of diamond films is spreading to disparate applications, like coatings for seals [9] or microelectromechanical systems [5], where low friction is crucial.

The friction properties of polycrystalline diamond films have been studied under various experimental environments [10–14] and shown to be sensitive to preparation and environmental conditions. Surface roughness, relative humidity, gases, and lubricants can alter the friction coefficient by orders of magnitude. However, smooth diamond films are able to exhibit ultralow friction in common environments [12–14]: little water vapor in air can drop the friction coefficient to 0.01 [13].

In general, a precondition for ultralow friction is the absence of strong chemical bonds between the sliding surfaces [15]. Diamond surfaces are usually H/OH passivated, due to contact with environmental molecules prior to sliding [14,16]. Mechanical rubbing can produce surface dangling bonds (DBs) and C—C bonds across the sliding interface. A fast surface repassivation is necessary to reestablish the conditions for ultralow friction.

Two repassivation mechanisms were proposed for the ultralow friction of diamond: rehybridization [11,17] and chemical termination [12–14]. In the former case, low friction is ascribed to graphitization at the sliding interface. It was argued, however, that the $sp^3$-to-$sp^2$ rehybridization can be the result of shear-induced amorphization [18,19] and does not contribute to lubrication [12]. The latter mechanism is less controversial and supported by many experiments and simulations. Friction and wear of diamond are lower in humid environments than in dry air or ultrahigh vacuum [12]. Density-functional theory (DFT) molecular dynamics (MD) simulations [20] showed that water molecules confined between sliding diamond (100) surfaces undergo dissociative chemisorption, thus passivating the surfaces.

In this Letter we report the results of large-scale density-functional tight-binding (DFTB) [21,22] MD simulations of diamond surfaces in contact with water and provide validation of the results by DFT calculations when necessary. Instead of modelling the (100) surface orientation [14,20], we focus on the (111) surface. The latter is known to be the natural cleavage plane of diamond, not prone to extensive mechanical amorphization [18], and thus likely to be found on diamond films. The computational efficiency of DFTB allows us to extend the ∼10 ps [20] time scale of DFT-MD to ∼0.2 ns and to perform a systematic study of friction for increasing quantities of water. As a result, our relatively simple model provides deep insight into the surprisingly diverse atomic-scale mechanisms governing friction of diamond under dry and humid conditions.

Specifically, starting from a dry diamond-diamond contact and increasing the amount of confined water, we observe the following (Fig. 1): (I) cold welding of the two surfaces via C—C bonds followed by mechanical amorphization, (II) cold welding via C—O—C bridges without amorphization, (III) aromatic passivation via Pandey surface reconstruction [23], (IV) water dissociative chemisorption and H/OH surface passivation, and (V) formation of water layers between the H/OH-passivated surfaces. These results unveil previously unreported atomic-scale friction mechanisms of water-lubricated diamond surfaces. First, interfacial ether groups play a crucial role as they can either cause cold welding or trigger the Pandey surface reconstruction. Secondly, the passivation of the surfaces does not necessarily rely on chemical H/OH termination and can occur via water-induced Pandey

 

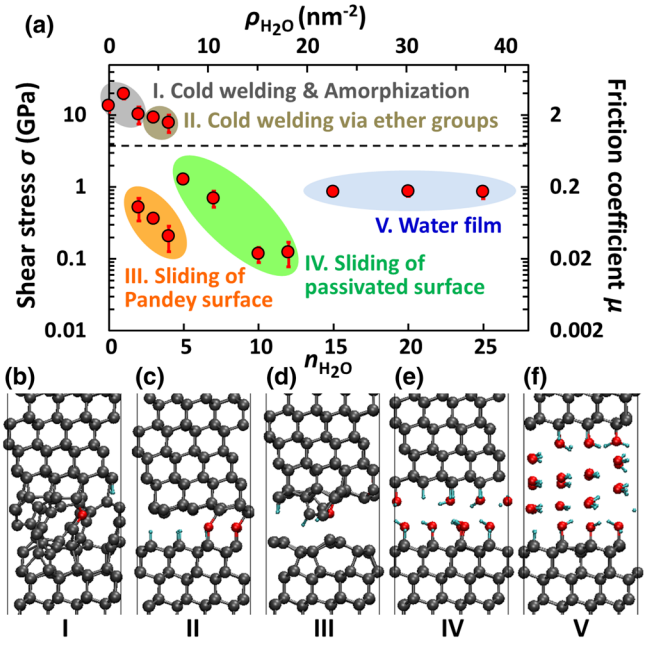


FIG. 1. (a) Frictional shear stress $\sigma = (\langle F_F \rangle / l_x l_y)$ and friction coefficient $\mu = (\sigma / P_N)$ as a function of $n_{H_2O}$ and $\rho_{H_2O} = (n_{H_2O} / l_x l_y)$ for two initially nonreconstructed diamond (111) surfaces with $l_x$ and $l_y$ being the lateral periodic box size in and perpendicular to sliding direction, respectively. After 0.1 ns, the friction forces $F_F(t)$ are averaged during time intervals $t_x = (l_x / v)$. Red circles represent averages over five $t_x$ periods and error bars are corresponding standard deviations. Panels (b) to (f) show representative snapshots for regimes I–V at $t = 0.1$ ns (with $n_{H_2O} = 1, 3, 2, 10$ and 25, respectively). Gray, red, and cyan spheres represent carbon, oxygen, and hydrogen atoms, respectively.

reconstruction. Such aromatic structure can sustain high loads (>5 GPa) even under dry sliding and lean water lubrication, thus suggesting aromatic passivation as an alternative explanation for diamond's ultralow friction under boundary lubrication. Finally, at higher water coverage, chemical passivation is accomplished by dense H/OH surface terminations, which frequently rely on Grotthuss-type diffusion [24] of $H_3O^+$ and $OH^-$ ions in water. These tribochemical reactions and the resulting surface structures are relevant to a broad range of tribological systems and are important ingredients to generate realistic surface models for large-scale, nonreactive MD simulations of water-lubricated covalent materials [25–28].

To build our model systems, we start from the unreconstructed diamond (111) surface with one DB per topmost carbon atom [29]. Two diamond slabs (each composed of 12 layers with 12 carbon atoms per layer and a hydrogen-terminated outermost layer) are brought into sliding contact. The terminating H atoms and the two outermost layers of the top and bottom slabs are held rigid. The rigid layer of the upper slab is moved at a constant velocity $v = 100$ m/s under a normal pressure $P_N = 5$ GPa. The system temperature $T$ is kept constant at 300 K using a Langevin thermostat [30] (see Supplemental Material [31] for further details).

First, we perform sliding simulations of two nonreconstructed (NR) diamond (111) surfaces in contact with an increasing number of water molecules ($n_{H_2O} = 0$–25). Interestingly, the frictional shear stress $\sigma$ strongly varies with $n_{H_2O}$ [Fig. 1(a)] and five friction regimes can be observed. The friction regimes I–V can be distinguished by characteristic structural patterns in the diamond-diamond and diamond-water-diamond interfaces [see representative configurations at $t = 0.1$ ns in Figs. 1(b)–1(f) and supplemental movies [31]] and can be divided into two classes [dashed horizontal dividing line in Fig. 1(a)]: regimes with cold welding (CW, i.e., I and II) and regimes without interfacial covalent bonding [not cold welding (NCW) regimes III–V].

For $n_{H_2O} \leq 2$ (corresponding to a water surface density $\rho_{H_2O} = 4$ nm$^{-2}$) C—C bonds and C—O—C groups form between the surfaces before the onset of sliding. During sliding, amorphization occurs at the interface [regime I, Fig. 1(b)]. These results are consistent with MD simulations [18] that also showed amorphization for $n_{H_2O} = 0$ and a frictional shear stress of the order of 10 GPa. Regime I results in the highest friction among all the five regimes. Also for $n_{H_2O} = 3$ and 4 initial cold welding is observed. However, only ether groups connect the two surfaces and no amorphization is detected [regime II, Fig. 1(c)]. While the presence of only ether groups at the sliding interface slightly reduces the friction, the shear stress is still of the order of 10 GPa.

Interestingly, some of the simulations with $2 \leq n_{H_2O} \leq 4$ result in the Pandey reconstruction [23] of one of the two diamond (111) surfaces [regime III, Fig. 1(d)]. In regime III, no interfacial covalent bonds form within the simulation time due to the threefold graphitelike coordination and aromatic $\pi$-bonded chains on the Pandey-reconstructed (PR) surface [23]. As a result, friction is 2 orders of magnitude lower than in the CW regime in spite of the small amount of water.

For $5 \leq n_{H_2O} \leq 12$, two partially or fully H/OH-passivated surfaces are in sliding contact [regime IV, Fig. 1(e)]. The H/OH surface termination coverages $\theta_{H/OH}$ are 0.42, 0.58, 0.83, and 1.00 after 0.1 ns, for $n_{H_2O} = 5, 7, 10$ and 12, respectively [44]. In agreement with previous works [12,13], H/OH surface termination promotes an ultralow friction regime. The lowest friction coefficient in regime IV is 0.02 for $n_{H_2O} = 10$ (quantitative justification of this value is given in Supplemental Material [31]). For $n_{H_2O} \geq 15$, both surfaces are almost completely H/OH terminated and a nanoscale water film forms between the surfaces [regime V, Fig. 1(f)]. In this regime, friction increases slightly—presumably due to stick slip caused by lubricant submonolayer coverage [45] or other viscous effects [46].

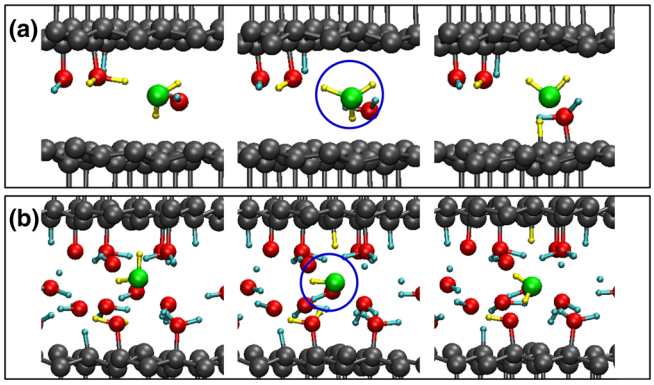


FIG. 2. Examples of surface passivation via proton transport mediated by (a) $H_3O^+$ and (b) $OH^-$ ions. The two ions are encircled in each middle panel. Green and yellow spheres represent the oxygen and hydrogen atoms involved, respectively.

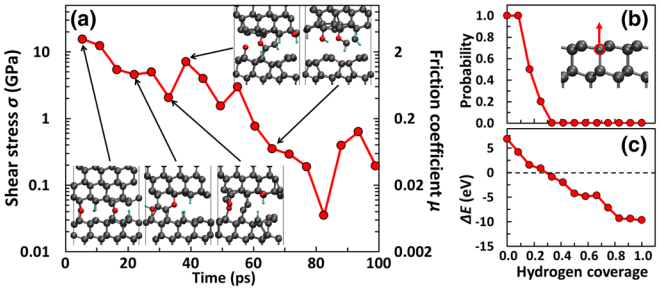


FIG. 3. (a) Evolution of frictional shear stress $\sigma$ and friction coefficient $\mu$ for $n_{H_2O} = 3$. Insets show characteristic configurations (supplemental movie S3 [31]). (b) Probability for the transition from the NR to the PR diamond (111) surface as a function of the hydrogen coverage $\theta_H$. The transition is triggered by pulling a second-layer carbon atom (inset). (c) Energy difference $\Delta E = E_{NR} - E_{PR}$ between the NR and PR surfaces as a function of $\theta_H$.

Regimes IV and V are a result of water dissociative chemisorption. We observe two possible mechanisms for the H/OH surface passivation: (i) direct dissociative chemisorption of $H_2O$ and (ii) long-range $H_2O$ dissociation mediated by the transport of hydrated $H_3O^+$ and $OH^-$ ions [24]. While the former has already been suggested [10,18], the latter has not been reported yet in a tribological context. Figure 2 shows examples of surface passivation via transport of $H_3O^+$ (Grotthuss mechanism) and $OH^-$ ions. The $H_3O^+$-based mechanism begins with the chemisorption of a $H_2O$ molecule [Fig. 2(a)] via its O atom. Another $H_2O$ molecule abstracts a proton from the chemisorbed $H_2O$, resulting in a $H_3O^+$ ion. The excess proton then is transferred to the lower surface. Conversely, the $OH^-$-based mechanism begins with the proton transfer from a $H_2O$ molecule to an upper surface C atom [Fig. 2(b)]. The resulting $OH^-$ takes a proton from a chemisorbed $H_2O$ that subsequently becomes an OH termination on the lower surface. Surface passivation via ionic transport becomes essential as $\theta_{H/OH}$ increases on both countersurfaces and the presence of two neighboring DBs becomes less likely. In this case, direct dissociative chemisorption is strongly suppressed and a Grotthuss-type transport is essential as it bridges the gap between distant DBs.

Interestingly, surface chemical termination is not always necessary for establishing a low-friction, NCW regime. This is the case for regime III, which is unexpected and deserves a deeper investigation. Upon tribological load, a small amount of water can trigger the Pandey reconstruction of the diamond surface. This leads to ultralow friction even at extremely low water coverages. The detailed mechanism can be explained by looking at the time evolution of $\sigma$ and the interfacial structure for $n_{H_2O} = 3$ [Fig. 3(a)]. At the beginning of sliding, two surfaces are chemically bonded via C—O—C bridges (similar to regime II). After 35 ps, two C atoms of the upper surface are pulled out from their lattice sites (reminiscent of an onset of amorphization in regime I) and the C dimer bridges the two surfaces. Subsequently, a C atom of the lower surface is pulled upward by an O atom, which distorts the surrounding lattice and produces five- and sevenfold rings. This process marks the onset of the Pandey reconstruction, which propagates over the lower surface as $\theta_{H/OH}$ decreases [in the third and fourth inset of Fig. 3(a), H atoms move from the lower to upper surface]. At $t = 75$ ps, the lower surface is fully reconstructed and unterminated while the upper surface is unreconstructed and partially terminated by C—H, C—OH, and C—O—C groups. The full reconstruction prevents covalent bonds between the surfaces and establishes a NCW regime. This transition is accompanied by a drastic friction reduction (from $\sigma \approx 20$ GPa at $t = 0$ ps to $\sigma \approx 0.3$ GPa at $t = 82$ ps).

An important prerequisite for the Pandey reconstruction is a sufficient number of DBs on the nonreconstructed (111) surface [47]. The reconstruction becomes energetically favorable when more than 70% of the DBs are unsaturated [47]. These conditions are met by prolonged heating at $T > 1000$ K resulting in H desorption. On the dehydrogenated surface, the Pandey reconstruction can already occur at 430 K [48]. Since in our simulations $T$ stays close to 300 K, surface bond breaking cannot be thermally assisted but must be initiated by sliding—as shown in Fig. 3(a). Thus, we hypothesize that the surface transition is triggered by shear-induced tensile stretching of surface C—C bonds.

To test this hypothesis, a nonreconstructed surface with a random distribution of $n_H$ hydrogen atoms (corresponding to a hydrogen coverage $\theta_H$) is considered as an initial configuration. One of the second-layer carbon atoms is randomly chosen and pulled upwards to mimic the pulling forces exerted by the countersurface [inset of Fig. 3(b)]. Ten MD trajectories with different H positions are generated for each $\theta_H$. While low $\theta_H$ leads to surface reconstruction for all trajectories, no surface transition occurs when $\theta_H > 0.3$ [Fig. 3(b)], in agreement with the relative energetic stability of the two surfaces [Fig. 3(c)].

One can consider a scenario in which two water-lubricated polycrystalline diamond surfaces with preferential (111) texture [4] are brought in sliding contact. Let us assume that the surfaces experience humidity prior to sliding (resulting in global H/OH passivation) and that the applied load is sufficiently high to induce boundary lubrication of the initially nonreconstructed facets. For realistic topographies the majority of contacts form a finite gap between facets and therefore regimes IV and V are established. However, during asperity collision, gaps might be so small that the facets are depassivated by removal of H/OH terminations or even by cleavage along (111) planes. Depending on the degree of depassivation, the corresponding tribological contacts can remain in regime IV or undergo a transition into regimes I–III. Based on this scenario, it is conceivable that running in would extend Pandey-reconstructed zones on both counterbodies.

This represents the motivation for our final simulations. The steady-state friction between two Pandey-reconstructed surfaces interacting with different water quantities ($n_{H_2O} = 0$–25) is reported in Fig. 4(a). For all $n_{H_2O}$, neither water splitting nor cold welding occur at $P_N = 5$ GPa. Contrary to the unreconstructed (111) surfaces, low friction is achievable even in the absence of water [Fig. 4(b)]. Small amounts of water ($1 \leq n_{H_2O} \leq 4$) induce pronounced stick-slip motion that increases friction slightly [Fig. 4(c)]. For $n_{H_2O} \geq 5$, water layers form and stick-slip motion disappears. The lowest frictional shear stress is obtained for $n_{H_2O} = 7$. These results suggest that sliding of the two Pandey-reconstructed surfaces without H/OH termination display ultralow friction both in humid and dry conditions.

Interestingly, the Pandey reconstruction was reported as a seed for larger aromatic structures on diamond (111) surfaces [49], where thermal hot spots can cause graphitization [11]. To estimate the frictional properties of such structures, we consider the sliding contacts depicted in Figs. 4(d) and 4(e). In Fig. 4(d), a dome-shaped surface forms when some of the C—C bonds between the first and second bilayers are broken. A Pandey reconstruction on the second bilayer prevents the dome from going back to the original surface [49]. In Fig. 4(e), the remaining C—C bonds between the first and second bilayers are broken and bilayer graphene forms between two Pandey-reconstructed surfaces. Both structures lead to a further friction reduction compared to two dry Pandey-reconstructed surfaces [Fig. 4(a)].

In all the simulations of Fig. 4(a), the Pandey-reconstructed surface is found to be surprisingly stable at $P_N = 5$ GPa. While many studies documented the quality of DFTB for equilibrium properties of C—H—O systems [8,31,50], an assessment of its accuracy for these high-pressure conditions is needed. We thus study the stability of two Pandey-reconstructed surfaces separated by $n_{H_2O} = 0$, 1, and 6 $H_2O$ molecules with DFT (details in Supplemental Material [31]). Figure 4(f) shows $P_N$ as a function of the surface separation. For $n_{H_2O} = 0$, a NCW regime (blue squares) can be observed for amazingly high pressure ($P_N < 120$ GPa) followed by CW at $P_N > P_{CW} = 120$ GPa (blue diamonds). For $n_{H_2O} = 1$ and large surface separation, the $H_2O$ molecule is confined between the two surfaces with neither dissociation nor chemisorption (red squares). When the two surfaces get closer, the $H_2O$ molecule splits into H and OH (red circles). The critical pressure $P_S$ for splitting an isolated $H_2O$ molecule is 6 GPa. The two Pandey-reconstructed surfaces cold weld via an ether group at $P_N > P_{CW} = 28$ GPa (red diamonds). For $n_{H_2O} = 6$, $P_S$ increases to 48 GPa and cold welding occurs at $P_N > P_{CW} = 125$ GPa. Even in the presence of water the Pandey reconstruction prevents water splitting for $P_N < 6$ GPa or CW for $P_N < 28$ GPa. This result validates the high stability of sliding Pandey surfaces at $P_N = 5$ GPa in our DFTB simulations. Given that $P_{CW}$

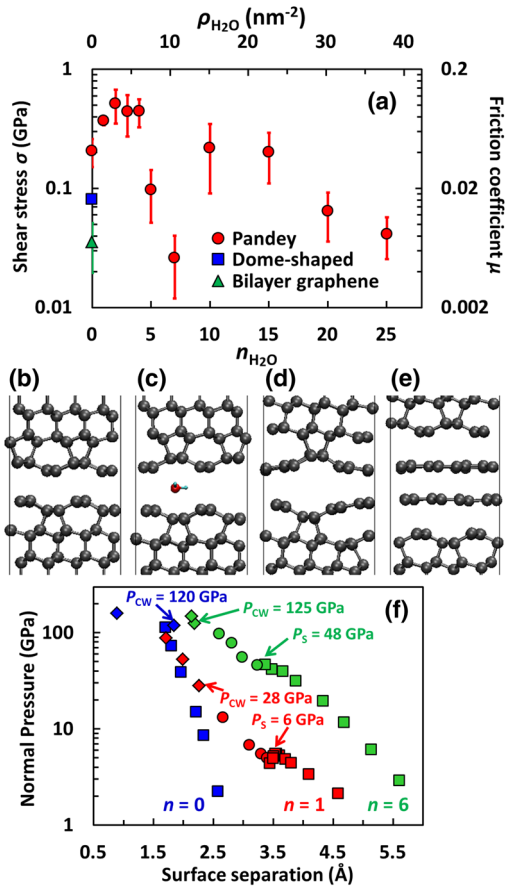


FIG. 4. (a) Frictional shear stress $\sigma$ and friction coefficient $\mu$ as a function of $n_{H_2O}$ for a Pandey-reconstructed diamond (111) surface with $P_N = 5$ GPa. Snapshots at $t = 0.1$ ns for (b) $n_{H_2O} = 0$ and (c) 1. Snapshots of graphitized surfaces: (d) dome-shaped surfaces [49] and (e) a bilayer graphene. (f) Normal pressure as a function of the surface separation for $n_{H_2O} = 0$ (blue), 1 (red), and 6 (green) by DFT calculations. Symbol shapes distinguish the interfacial configurations: squares, no structural change; circles, water splitting; diamonds, cold welding.

is significantly larger than experimentally observed contact pressures (1–5 GPa) [51], the Pandey-reconstructed surface is likely to play an important role in reducing friction between asperities in both humid and almost dry conditions.

In conclusion, this Letter reports hitherto unknown friction regimes for diamond (111) surfaces. Most regimes are transferable to other diamond surface orientations (Supplemental Material [31]), polycrystalline diamond, diamondlike carbon (DLC), and even to other covalent materials (e.g., silicon): Regime I is characterized by mechanical amorphization or rehybridization, which occurs on all diamond surfaces [18], H-free DLC films [52], and silicon surfaces [53]; regimes II, IV, and V are general consequences of the oxygen divalency and can be found on any covalently bonded surface; Grotthuss-type mechanisms for long-range H/OH transport should occur on any reactive water-splitting surface.

Only regime III is special, since the Pandey reconstruction is unique to diamond and silicon (111) surfaces [54]. However, Pandey-reconstructed silicon (111) surfaces lack aromaticity. Accordingly, they cold weld without external loads (Supplemental Material [31]) and therefore friction reduction by tribo-induced aromatic Pandey reconstruction is a unique feature of the diamond (111) surface. Nevertheless, other tribo-induced aromatic terminations could lead to a generalized regime III' (aromatic regime) resulting in friction reduction between $sp^2$ amorphous carbon layers supported by diamond [18] or H-free DLC [52].

T. K. acknowledges financial support by JSPS Overseas Research Fellowships. The authors gratefully acknowledge the computing time granted by the John von Neumann Institute for Computing (NIC) and provided on the supercomputer JURECA at Jülich Supercomputing Centre (JSC). G. M. and M. M. acknowledge fruitful discussions with Lars Pastewka, Martin Dienwiebel, and Robert Carpick and funding by the industrial board of the MicroTribology Center $\mu$TC. M. M. is grateful for funding by the Deutsche Forschungsgemeinschaft within Grant No. Mo879/17.

*Corresponding author.
michael.moseler@iwm.fraunhofer.de

[1] A. Ersoy and U. Atici, Diam. Relat. Mater. **13**, 22 (2004).
[2] A. Köpf, S. Feistritzer, and K. Udier, Int. J. Refract. Met. Hard Mater. **24**, 354 (2006).
[3] J. R. Hird and J. E. Field, Proc. R. Soc. A **460**, 3547 (2004).
[4] A. Schade, S. M. Rosiwal, and R. F. Singer, Diam. Relat. Mater. **15**, 1682 (2006).
[5] A. V. Sumant, O. Auciello, R. W. Carpick, S. Srinivasan, and J. E. Butler, MRS Bull. **35**, 281 (2010).
[6] O. A. Williams, Diam. Relat. Mater. **20**, 621 (2011).
[7] E. L. H. Thomas, G. W. Nelson, S. Mandal, J. S. Foord, and O. A. Williams, Carbon **68**, 473 (2014).
[8] A. Peguiron, G. Moras, M. Walter, H. Uetsuka, L. Pastewka, and M. Moseler, Carbon **98**, 474 (2016).
[9] J. Otschik, A. Schrüfer, J. Thelke, M. Kirchhof, and S. Schmaderer, World pumps **2010**, 18 (2010).
[10] I. P. Hayward, Surf. Coat. Technol. **49**, 554 (1991).
[11] A. Erdemir, G. R. Fenske, A. R. Krauss, D. M. Gruen, T. McCauley, and R. T. Csencsits, Surf. Coat. Technol. **120**, 565 (1999).
[12] A. R. Konicek, D. S. Grierson, P. U. P. A. Gilbert, W. G. Sawyer, A. V. Sumant, and R. W. Carpick, Phys. Rev. Lett. **100**, 235502 (2008).
[13] A. R. Konicek, D. S. Grierson, A. V. Sumant, T. A. Friedmann, J. P. Sullivan, P. U. P. A. Gilbert, W. G. Sawyer, and R. W. Carpick, Phys. Rev. B **85**, 155448 (2012).
[14] M. I. De Barros Bouchet, G. Zilibotti, C. Matta, M. C. Righi, L. Vandenbulcke, B. Vacher, and J. M. Martin, J. Phys. Chem. C **116**, 6966 (2012).
[15] L. Pastewka, S. Moser, and M. Moseler, Tribol. Lett. **39**, 49 (2010).
[16] O. Manelli, S. Corni, and M. C. Righi, J. Phys. Chem. C **114**, 7045 (2010).
[17] S. E. Grillo and J. E. Field, J. Phys. D **33**, 595 (2000).
[18] L. Pastewka, S. Moser, P. Gumbsch, and M. Moseler, Nat. Mater. **10**, 34 (2011).
[19] M. I. De Barros Bouchet, C. Matta, B. Vacher, T. Le-Mogne, J. M. Martin, J. von Lautz, T.-B. Ma, L. Pastewka, J. Otschik, P. Gumbsch, and M. Moseler, Carbon **87**, 317 (2015).
[20] G. Zilibotti, S. Corni, and M. C. Righi, Phys. Rev. Lett. **111**, 146101 (2013).
[21] D. Porezag, T. Frauenheim, T. Köhler, G. Seifert, and R. Kaschner, Phys. Rev. B **51**, 12947 (1995).
[22] M. Elstner, D. Porezag, G. Jungnickel, J. Elsner, M. Haugk, T. Frauenheim, S. Suhai, and G. Seifert, Phys. Rev. B **58**, 7260 (1998).
[23] K. C. Pandey, Phys. Rev. B **25**, 4338 (1982).
[24] M. E. Tuckerman, D. Marx, and M. Parrinello, Nature (London) **417**, 925 (2002).
[25] C. D. Lorenz, J. M. D. Lane, M. Chandross, M. J. Stevens, and G. S. Grest, Langmuir **25**, 4535 (2009).
[26] L. Ramin and A. Jabbarzadeh, Langmuir **29**, 13367 (2013).
[27] M. Rullich, V. C. Weiss, and T. Frauenheim, Model. Simul. Mater. Sci. Eng. **21**, 055027 (2013).
[28] L. B. Krott and M. C. Barbosa, Phys. Rev. E **89**, 012110 (2014).
[29] D. Petrini and K. Larsson, J. Phys. Chem. C **112**, 3018 (2008).
[30] D. Frenkel and B. Smit, *Understanding Molecular Simulations: From Algorithms to Applications*, 2nd ed. (Academic Press, New York, 2001).
[31] See Supplemental Material at http://link.aps.org/supplemental/10.1103/PhysRevLett.119.096101 for the details of the computational setup for DFTB MD and DFT calculations and simulation movies, which includes Refs. [32–43].
[32] M. Weinert and J. W. Davenport, Phys. Rev. B **45**, 13709 (1992).
[33] J. A. Harrison, C. T. White, R. J. Colton, and D. W. Brenner, Phys. Rev. B **46**, 9700 (1992).
[34] J. Gao, W. D. Luedtke, D. Gourdon, M. Ruths, J. N. Israelachvili, and U. Landman, J. Phys. Chem. B **108**, 3410 (2004).

[35] A. Berman, C. Drummond, and J. Israelachvili, Tribol. Lett. **4**, 95 (1998).
[36] Y. Mo, K. T. Turner, and I. Szlufarska, Nature (London) **457**, 1116 (2009).
[37] P. Maksyutenko, T. R. Rizzo, and O. V Boyarkin, J. Chem. Phys. **125**, 181101 (2006).
[38] M. W. Palascak and G. C. Shields, J. Phys. Chem. A **108**, 3692 (2004).
[39] N. Goldman, R. S. Fellers, M. G. Brown, L. B. Braly, C. J. Keoshian, C. Leforestier, and R. J. Saykally, J. Chem. Phys. **116**, 10148 (2002).
[40] P. Giannozzi *et al.*, J. Phys. Condens. Matter **21**, 395502 (2009).
[41] D. Vanderbilt, Phys. Rev. B **41**, 7892 (1990).
[42] J. P. Perdew, K. Burke, and M. Ernzerhof, Phys. Rev. Lett. **77**, 3865 (1996).
[43] H. J. Monkhorst and J. D. Pack, Phys. Rev. B **13**, 5188 (1976).
[44] The surface coverage $\theta$ is defined as the ratio of the number of H/OH-terminated surface carbon atoms to the total number of surface carbon atoms.
[45] G. He, M. H. Müser, and M. O. Robbins, Science **284**, 1650 (1999).
[46] A. Opitz, S. U. Ahmed, J. A. Schaefer, and M. Scherge, Surf. Sci. **504**, 199 (2002).
[47] J. B. Cui, J. Ristein, and L. Ley, Phys. Rev. B **59**, 5847 (1999).
[48] G. Kern, J. Hafner, and G. Kresse, Surf. Sci. **366**, 445 (1996).
[49] G. Kern and J. Hafner, Phys. Rev. B **58**, 13167 (1998).
[50] T. Kuwahara, H. Ito, K. Kawaguchi, Y. Higuchi, N. Ozawa, and M. Kubo, J. Phys. Chem. C **120**, 2615 (2016).
[51] G. Gao, R. J. Cannara, R. W. Carpick, and J. A. Harrison, Langmuir **23**, 5394 (2007).
[52] T. Kunze, M. Posselt, S. Gemming, G. Seifert, A. R. Konicek, R. W. Carpick, L. Pastewka, and M. Moseler, Tribol. Lett. **53**, 119 (2014).
[53] Z. Zhang, D. Guo, B. Wang, R. Kang, and B. Zhang, Sci. Rep. **5**, 16395 (2015).
[54] K. C. Pandey, Phys. Rev. Lett. **47**, 1913 (1981).